Check for updates

Super-stable SnO$_2$/MoS$_2$ enhanced the electrocatalytic hydrogen evolution in acidic environments†

Kun Huang,‡[a] Lan Yang,‡[a] Yihong Gao,[a] Shikuo Li,*[b] Hui Zhang [ID] *[b] and Fangzhi Huang [ID] *[a]

For electrocatalytic hydrogen evolution in acidic environments, the stability of catalysts has always been a significant factor restricting development. Here, we prepared a superstable SnO$_2$/MoS$_2$ coupled nanosheet array on carbon cloth (CC@SnO$_2$/MoS$_2$), exhibiting an overpotential of 166 mV at a current density of 10 mA cm^{-2}. According to the results of various tests and theoretical calculations, it is shown that the establishment of SnO$_2$/MoS$_2$ interface engineering is to accelerate the electron transmission on the heterogeneous interface and S defects on the edge of MoS$_2$, and finally improve the conductivity and catalytic activity of the catalyst. More importantly, the formation of an SnO$_2$ interface layer during *in situ* transformation improves the stability and hydrophilicity of the material surface. We have proposed a strategy for engineering an interface with fast electron transport and proton adsorption, providing some new ideas for the design of HER catalysts in acid electrolytes.

Introduction

Benefiting from the advantages, a pollution-free and simple equipment, electrocatalytic hydrogen evolution technology is expected to replace the current industrial hydrogen production technology with high pollution and consumption.[1–5] However, high-performance HER electrocatalysts expected to industrialization are precious metals such as Pt, which cannot acheive production with large scale due to their rareness at present.[6,7] Therefore, non-noble metal based electrocatalysts with high efficiency are urgently needed in the field of electrocatalytic hydrogen production.[8,9] Compared with basic electrolytes, acidic electrolytes contain a large amount of free H$^+$, which is more conducive to the occurrence of the electrocatalytic hydrogen evolution reaction.[10–12] Unfortunately, the stability of most transition metal electrocatalysts in acidic solutions is so insufficient that the research of acidic HER catalysts is behind that of alkaline catalysts.[13,14] Therefore, it is of practical value to develop non-noble metal electrocatalytic HER catalysts in acidic electrolytes.[15–17] Some strategies have been developed to prepare acidic HER catalysts with low

consumption or no precious metals.[18,19] Liu *et al.* prepared a single-atom Pt catalyst on the surface of amorphous MoO$_3$ and performed the HER in an acidic environment.[20] The construction of monoatomic Pt contributes to the low consumption of precious metals and high performance, and the acid resistance of MoO$_3$ can improve the corrosion resistance of the material.[21–23] Using acid-resistant materials such as carbon materials to provide a protective layer for some transition metal semiconductors or materials is another promising strategy.[24–27] However, instability and cumbersome problems in the preparation process will exist in the above strategies.[13,28] Perhaps another way to think about it is that exploring materials with excellent intrinsic properties of acid resistance is an effective strategy to avoid the above triviality and instability.[29–33]

Molybdenum disulfide (MoS$_2$) has excellent acid resistance, electrochemical properties and abundant reserves, and has been widely used in the field of electrocatalysis.[34,35] Its catalytic activity is mainly derived from the unsaturated S atom edge of its layered structure, as shown in some reports.[36–40] Therefore, increasing the edge part of MoS$_2$ is an effective way to improve its catalytic performance. It has been reported that changing the morphology of molybdenum disulfide, such as nanoplatelets, nanoparticles, and quantum dots, expands the number of edges.[30,31,41] Among them, dispersing MoS$_2$ nanoparticles on an acid-resistant nanosheet array is a feasible method to increase the number of unsaturated S atoms and prevent the aggregation.[30] Secondly, it is possible to construct the defects and vacancies of MoS$_2$ to increase the degree of unsaturation at the

[a]*School of Chemistry and Chemical Engineering, Anhui University, Hefei, Anhui 230601, P. R. China. E-mail: huangfangzhi@163.com*

[b]*School of Materials Science and Engineering, Anhui University, Hefei, Anhui 230601, P. R. China. E-mail: lishikuo@ahu.edu.cn; zhhui@ahu.edu.cn*

† Electronic supplementary information (ESI) available. See https://doi.org/10.1039/d2ra03627d

‡ Contributed equally to this work.

edge of the S atom, thereby increasing the number of active sites. The research of Baker *et al.* showed that the competitive reaction between metal ions (such as Mo^{4+} and Sn^{4+}) and non-metals in the *in situ* conversion process can effectively produce more defects.[42] Finally, the resistance of electron transfer between the layers of MoS_2 leads to poor conductivity and activity, which hinders the catalytic performance.[43,44] The electron injection of the conductive medium into the molybdenum disulfide can effectively reduce this resistance.[30,45] In summary, growing MoS_2 nanoparticles on a nanosheet array with high conductivity and strong corrosion resistance through the competitive reaction of ions in the solution is a promising strategy. The thus obtained SnO_2/MoS_2 interface layer with fast electron transfer and proton adsorption is expected to be developed as a highly efficient and stable non-noble metal self-supporting HER electrocatalyst in acidic electrolytes.

Following the above idea, we used SnS_2 grown on carbon cloth as a precursor, and MoS_2 particles were grown on it to obtain a SnO_2/MoS_2 coupled nanosheet array. First, the uniform distribution of MoS_2 nanoparticles on the nanosheets and the conversion of sulfides to oxides during the reaction increase the number of MoS_2 unsaturated sulfur defects; secondly, the good hydrophilicity and stability of the SnO_2 nanosheet substrate enhanced the hydrophilicity and stability of the catalyst;[46] the heterogeneous interface layer formed by the coupling of SnO_2 and MoS_2 can accelerate the injection of electrons into MoS_2 and reduce the resistance to electron transfer between molybdenum disulfide layers. The SnO_2/MoS_2 heterogeneous nanosheet arrays obtained by us maintain good activity and stability in acidic electrolytes. At a current density of 10 mA cm^{-2}, the overpotential is 166 mV, which is significantly lower than that of pure MoS_2 and SnO_2. In the 0.5 M H_2SO_4 electrolyte, the catalyst can be utilized for more than 20 hours, accompanied by a current density decay within an acceptable range (less than 20%). Experimental results have proved that our proposed strategy of constructing an interface layer in designing an efficient and stable non-noble metal self-supporting HER electrocatalyst in an acidic electrolyte is effective and promising.

Experimental

Chemicals and materials

WOS1009 carbon cloth (CC) was purchased from Taiwan CeTech Co., Ltd. Other chemicals were of analytical grade and used as received without further purification. They were purchased from Shanghai Aladdin Biochemical Technology Co., Ltd and Sinopharm Chemical Reagent Co., Ltd. Ultrapure water was used throughout the experiments.

Pretreatment of carbon cloth

The conductive carbon cloth was soaked in concentrated nitric acid and allowed to stand for three days. The soaked carbon cloth was rinsed three times with ultrapure water, and different solvents were used for ultrasonic cleaning for 10 minutes. The obtained carbon cloth was soaked in absolute ethanol for later use.

Synthesis of CC@SnS$_2$ NSs

The typical synthesis process of CC@SnS$_2$ nanosheets is conducted by the solvothermal method. 140 mg of SnCl$_4\cdot$5H$_2$O was dissolved in 20 mL of absolute ethanol, and then 60.4 mg of TAA (thioacetamide) was added and rotated for 20 min. The resulting liquid was injected into a 50 mL reactor. The treated carbon cloth was leaned against the bottom of the reaction kettle so that the carbon cloth was completely immersed in the solution, which was placed in an oven to react at 100 °C for 6 h, and then cooled naturally. The obtained sample was washed three times with water and C$_2$H$_5$OH each. The finally obtained CC@SnS$_2$ nanosheets were activated in a vacuum drying oven at 70 °C for 12 h.

Synthesis of CC@SnO$_2$@MoS$_2$ NSs

CC@SnO$_2$@MoS$_2$ nanosheets are synthesized by the hydrothermal method. 1 mL, 2 mL, 3 mL and 4 mL of 1.44 mg mL^{-1} TAA ethanol solution were injected into four clean beakers in turn. Then, 1 mL, 2 mL, 3 mL and 4 mL of 4.84 mg mL^{-1} molybdate solution were added, respectively. After mixing, the above solutions were diluted to 20 mL with ethanol respectively. The above solution was transferred to four 50 mL reactors, and the synthesized CC@SnS$_2$ nanosheets were leaned against the bottom of the reactor to completely immerse the carbon cloth in the solution. The reaction was carried out at 200 °C for 12 h. After cooling down, the obtained sample was washed with water and C$_2$H$_5$OH three times each. The finally obtained CC@SnO$_2$@MoS$_2$ nanosheets were dried in a vacuum drying oven at 70 °C for 12 h. The different samples obtained were named CC@SnO$_2$@MoS$_2$-1, CC@SnO$_2$@MoS$_2$-2.5, CC@SnO$_2$@MoS$_2$-5, and CC@SnO$_2$@-MoS$_2$-10.

Synthesis of CC@MoS$_2$ NSs

The synthesis of CC@MoS$_2$ nanosheets is roughly the same as the above CC@SnO$_2$@MoS$_2$-5 nanosheets except just replacing CC@SnS$_2$ with conductive carbon cloth.

Synthesis of CC@SnO$_2$ NSs

The solvothermal method was used to prepare CC@SnO$_2$ NSs. 140 mg of SnCl$_4$ 5H$_2$O and the corresponding Na$_3$C$_6$H$_5$O$_7$ 2H$_2$O were dissolved in 20 mL of distilled water. After stirring the solution for 5 minutes, a certain concentration of NaOH solution was added. The resulting liquid was injected into a 50 mL reactor. The treated carbon cloth was leaned against the bottom of the reaction kettle so that the carbon cloth was completely immersed in the solution, which was placed in an oven to react at 180 °C for 12 h, and then cooled naturally. The obtained sample was washed three times with water and C$_2$H$_5$OH each. The finally obtained CC@SnO$_2$ nanosheets were activated in a vacuum drying oven at 70 °C for 12 h.

Results and discussion

A schematic diagram of the material synthesis is shown in Scheme 1. First, SnS_2 NSs are constructed on the carbon cloth substrate using the solvothermal method. The thickness of the SnS_2 nanosheets is about 10 nm in the SEM image (Fig. 1A), growing uniformly and vertically on the carbon cloth.

The honeycomb-like porous structure of vertical array is open-type so that it is more conducive to the introduction of electrolytes. Subsequently, MoS_2 nanoparticles with uniform distribution and very uniform diameter were grown on the surface of SnS_2, as shown in Fig. 1B. SnS_2 will also be converted to SnO_2 at this time, which is confirmed in the following characterization analysis. In addition, some MoS_2 nanosheets will epitaxially grow along the edge of the SnO_2 nanosheets, which also exposes more MoS_2 unsaturated S edges. With the increase of S source and Mo source, MoS_2 on the surface of SnO_2 gradually transformed into nanoparticles, and finally formed multiple folds covering the surface, shown in the SEM of samples (Fig. S1A–D†). The SEM results indicate that the coverage of the folds from nanoparticles to MoS_2 on the substrate is controllable. The combination of MoS_2 nanoparticles and SnO_2 nanosheets can be clearly observed from the transmission electron microscope image (TEM), as shown in Fig. 1C. The uniformly distributed MoS_2 nanoparticles shown in the image will not agglomerate and have a diameter of about 25 nm. The high-magnification TEM of SnO_2/MoS_2 NSs clearly shows the lattice spacing of SnO_2 and MoS_2, as shown in Fig. 1D. The lattice spacing of SnO_2 is 0.245 nm and 0.316 nm, and the distribution corresponds to the (200) and (001) crystal planes. In addition, the crystal lattice fracture is clearly observed, which corresponds to the defects formed during the crystal phase transformation. The formation of these defects is closely related to the competitive reaction of non-metal elements in the solvothermal reaction process. The lattice spacing of 0.61 nm corresponds to the (002) crystal plane of MoS_2. The element distribution image of SnO_2/MoS_2

NSs shows that Sn, Mo, S, and O are evenly distributed on the nanosheet, which reveals the existence and distribution of each element, confirming the accomplished loading of MoS_2 (Fig. 1E).

The results of XRD prove that the phase change from sulfide to oxide actually occurred during the second step of the reaction (Fig. S2A†). However, due to the low content and poor crystallinity of MoS_2 on the surface as well as the strong peak of SnO_2, the corresponding diffraction peak of MoS_2 is difficult to find. In order to completely prove that the samples are loaded with MoS_2 and to research the details of the transition from SnS_2 to SnO_2, we performed Raman spectroscopy analysis with different reaction times (Fig. 2A). In the unreacted pure SnS_2 curve, a single strong Raman peak is observed at 317 cm^{-1}, which corresponds to the A_{1g} characteristic peak of SnS_2. When the reaction time is 3 h, the intensity of the characteristic peak corresponding to 317 cm^{-1} is significantly reduced, indicating that the SnS_2 composition is decreasing. Since Sn ions are more easily coordinated with oxygen in solution and are less sulfur-loving than Mo ions, the transformation of SnS_2 to SnO_2 has begun. However, the characteristic peak of MoS_2 is still not observed at this time, which reflects that the formation of MoS_2 requires more time or is later than the transformation of SnS_2. We prefer the former. As the formation reaction of MoS_2 has begun, the more sulfur-philic nature of Mo compared to Sn promotes the transition from SnS_2 to SnO_2 to occur more quickly. Accompanied by a reaction time of 6 h, the disappeared A_{1g} characteristic peak of SnS_2 indicates that the phase change from SnS_2 to SnO_2 has been completely completed. The E_{12g} in-plane and A_{1g} out-of-plane characteristic peaks corresponding to MoS_2 at 380 and 408 cm^{-1} indicate that MoS_2 has initially formed. With the reaction for 12 hours, the further enhanced characteristic peaks at 380 and 408 cm^{-1} corresponded to the complete transition from SnS_2 to SnO_2/MoS_2. The results of the Raman diagram indicate that the competition between Sn and Mo for
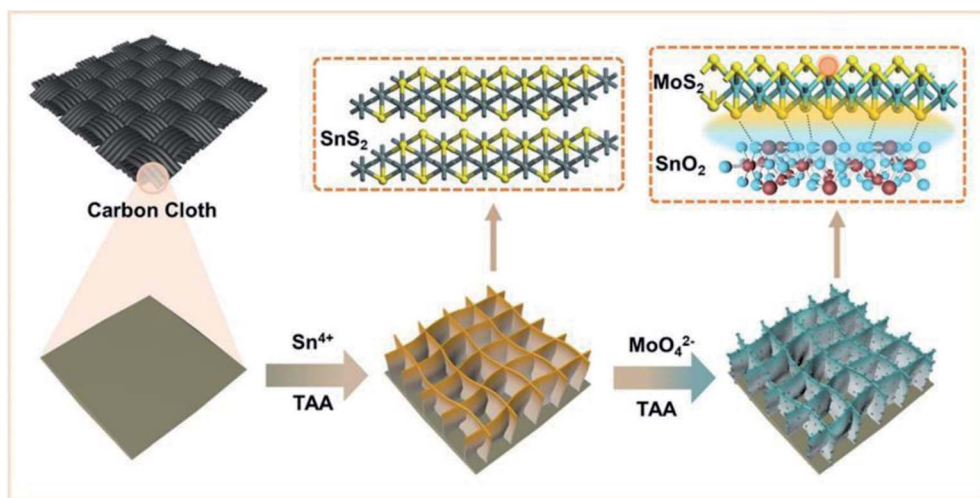
Scheme 1 Diagram of material synthesis.

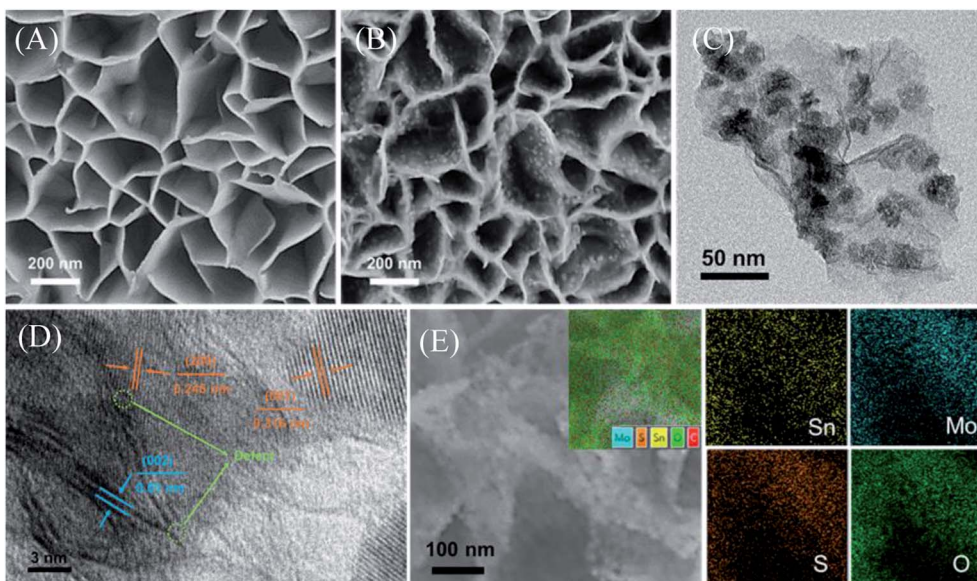**Fig. 1** (A) SEM image of CC@SnS$_2$ NSs. (B) SEM image of CC@SnO$_2$/MoS$_2$ NSs. (C) TEM images of SnO$_2$/MoS$_2$ NSs. (D) HRTEM images of SnO$_2$/MoS$_2$ NSs. (E) Element distribution mapping of Sn, Mo, S and O corresponding to SnO$_2$/MoS$_2$ NSs.

S^{2-} does exist during the reaction, which leads to the transformation of Sn from sulfide to oxide.

In order to further research the valence composition of typical SnO$_2$/MoS$_2$ nanosheets, we performed XPS characterization of the samples. The characteristic peaks of Mo and Sn further proved the successful preparation of SnO$_2$/MoS$_2$ nanosheets, shown in the XPS total spectrum (Fig. 2B). The high-resolution XPS spectra of each element in SnO$_2$/MoS$_2$ NSs
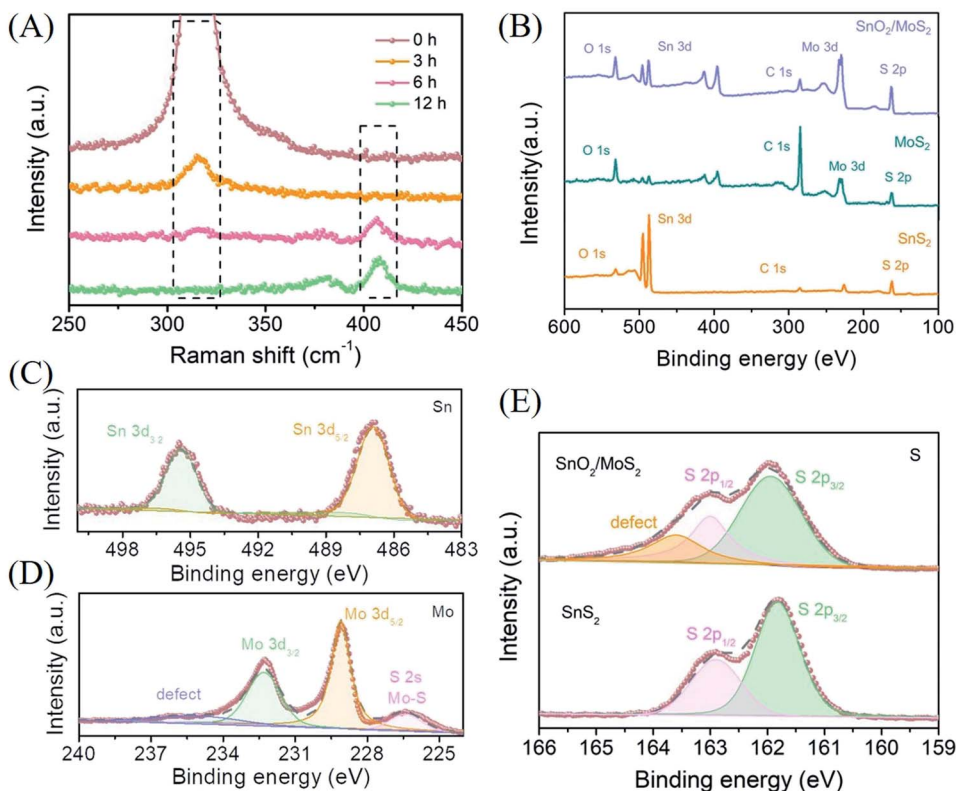

Fig. 2 (A) Raman image of different reaction times during the growth of MoS$_2$. (B) XPS general map of SnO$_2$/MoS$_2$ NSs. High resolution XPS image of SnO$_2$/MoS$_2$ NSs: (C) Sn in SnO$_2$/MoS$_2$ NSs, (D) Mo in SnO$_2$/MoS$_2$ NSs, and (E) S in SnO$_2$/MoS$_2$ NSs and SnS$_2$ NSs.

have been obtained (Fig. 2C–E). Sn $3d_{5/2}$ and Sn $3d_{3/2}$ located at 486.9 eV and 495.4 eV, respectively, are attributed to the characteristic peaks of Sn^{4+}, indicating the presence of positive tetravalent Sn elements in the material (Fig. 2C). The formation of MoS_2 is also certified by two characteristic peaks in the high-resolution XPS spectrum of Mo, as shown in Fig. 2D. The characteristic peaks at 229.1 eV and 232.3 eV correspond to Mo $3d_{5/2}$ and Mo $3d_{3/2}$, which confirms the above point. The S 2s energy peak near 226.4 eV is derived from the Mo–S bond, which once again verifies the existence of molybdenum disulfide. A broad peak can also be observed at 235.4 eV, which may be related to the defects in the competitive reaction. The characteristic peaks of S $2p_{2/3}$ and S $2p_{1/3}$ are observed at 161.96 eV and 163.0 eV, indicating that the valence states of S elements in SnS_2 and SnO_2/MoS_2 are all negative divalent (Fig. 2E). And a peak can be observed at 163.6 eV, which is attributed to the defects of the unsaturated sulfur atoms contained. The XPS results once again confirmed that we successfully synthesized the SnO_2/MoS_2 nanosheet structure, and the sample contains a large number of defects that can provide active sites due to the competitive reaction of metal ions for S^{2-}.

With a scan rate of 1 mV s^{-1}, CC@SnO$_2$/MoS$_2$ NS samples were tested for HER performance in 0.5 M H$_2$SO$_4$ electrolyte. The comparative samples are CC@Pt/C, CC@SnS$_2$, CC@SnO$_2$ and CC@MoS$_2$ with roughly the same load mass. All electrocatalytic results have been compensated for resistance to obtain accurate catalyst intrinsic performance. As shown in Fig. 3A, the

CC@SnO$_2$/MoS$_2$ NS-2.5 sample exhibits a current density of 10 mA cm^{-2} at an overpotential of only 166 mV, which is better than other comparative samples. Pt/C exhibits the best activity as a conventional HER catalyst with an overpotential of 90 mV. It is worth noting that the overpotential of CC@SnO$_2$/MoS$_2$ NSs-2.5 is the lowest, better than samples with other loadings (Fig. 3B). This means that only the most suitable load of MoS$_2$ can maximize performance. The CC@SnO$_2$ sample has poor electrocatalytic activity, which makes it difficult to measure the standard current density. Compared with CC@SnS$_2$ (494 mV) and CC@MoS$_2$ (330 mV), the overpotential of CC@SnO$_2$/MoS$_2$ NSs-2.5 has a voltage reduction of 330 mV and 164 mV, respectively. The Tafel slope of CC@SnO$_2$/MoS$_2$ NSs-2.5 is 68.49 mV dec^{-1}, which is much smaller than that of the other comparative samples, indicating that the CC@SnO$_2$/MoS$_2$ NS-2.5 sample has the most excellent electrochemical reaction kinetics among many materials (Fig. 3B). The results of LSV and Tafel slope show that we optimize electron transfer, proton adsorption and wettability of MoS$_2$ through designing the SnO$_2$/MoS$_2$ interface layer, which is reflected in the catalytic performance.

For electrocatalysts used in acid electrolytes, the stability is a significant parameter for evaluating catalysts. The i–t curve of the CC@SnO$_2$/MoS$_2$ sample was recorded with a voltage of 166 mV in order to test the stability of performance (Fig. 5A). After 20 hours of continuous electrolysis, samples with less than 20% attenuation of current indicate that the synthesized
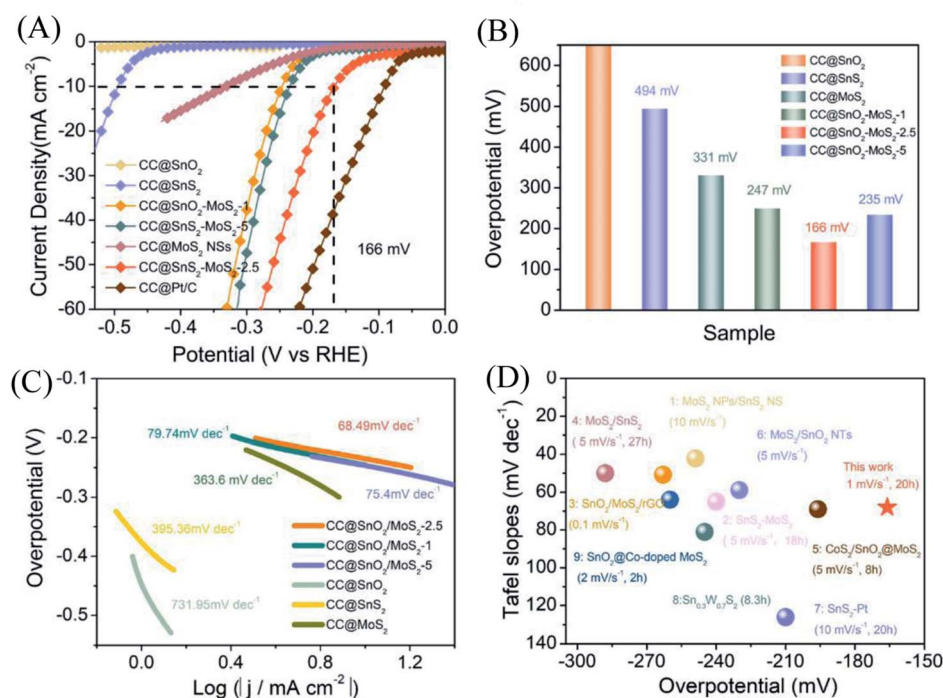

Fig. 3 (A) LSV curves of different SnO$_2$/MoS$_2$ NSs (1, 2.5, and 5), SnS$_2$, SnO$_2$, Pt/C and MoS$_2$ at 1 mV s^{-1}. (B) Overpotential (η) of different samples at 10 mA cm^{-2}. (C) Tafel slope plots corresponding to different samples. (D) A performance comparison diagram of this work with the work in 0.5 M H$_2$SO$_4$ of published relevant materials, with the sweep rate of the LSV curve and the stabilization time at 10 mA cm^{-2} in parentheses.[29–32,47–52]
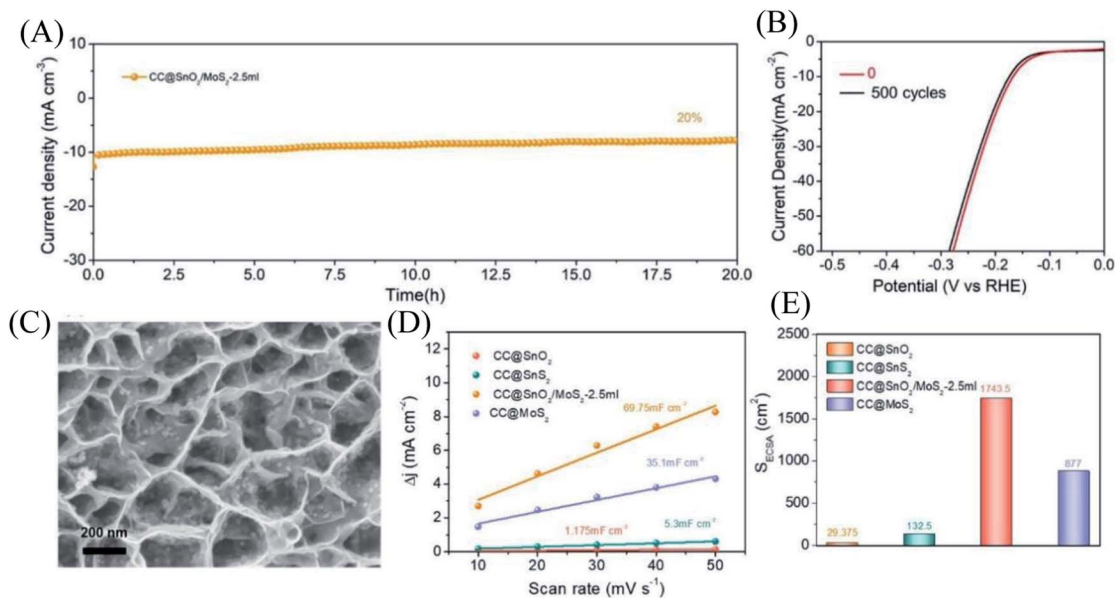
Fig. 4 (A) Curve of $i-t$ with a constant current density of 10 mA cm^{-2}. (B) LSV curve comparison of the SnO$_2$/MoS$_2$ NS-2.5 sample in 0 cycle and 500 cycles. (C) SEM image of SnO$_2$/MoS$_2$ NS-2.5 sample after 500 cycles. (D) The curve between CV scanning rate and current density of each sample. (E) The electrochemical active area of each sample.

CC@SnO$_2$/MoS$_2$ heterogeneous nanosheets are expected to achieve long-term electrocatalytic processes. The test of the continuous 500-cycle cyclic voltammetry curve without obvious attenuation shows that the catalyst can withstand continuous catalytic reactions of different potentials and shows good stability (Fig. 4B). The sample after 500 cycles maintained the original morphology and showed strong toughness (Fig. 4C). The performance of this work is compared with the reported performance of related materials 1–9, as shown in Fig. 3D.[29–32,47–52] The abscissa and ordinate of the graph are the overpotential of the catalyst at 10 mA cm^{-2} and the Tafel slope, respectively. The overpotential of the electrode material reported in this work is better than that of related materials, and its Tafel slope reflects that the electrochemical kinetics also has outstanding competitiveness. The electrochemical active area is usually an important basis for evaluating the intrinsic activity of a catalyst. The double-layer capacitor area of the material can be used to estimate the size of the electrochemically active area, as shown in Fig. S3.† The linear function image of the CV scan rate and current density difference (Δj) is obtained by fitting (Fig. 4E). From the figure, we can acquire that the C_{dl} of samples CC@SnO$_2$ NSs, CC@SnS$_2$ NSs, CC@MoS$_2$ NSs and CC@SnO$_2$/MoS$_2$ NSs-2.5 is 1.175, 5.3, 35.1 and 69.75 mF cm^{-2}, respectively. The electrochemically active area of the CC@SnO$_2$/MoS$_2$ NS-2.5 sample is 1743.5 cm^2, which is much higher than that of CC@MoS$_2$ NSs and other samples (Fig. 4F). On the basis of the above results, we also calculated ESCA-normalized LSV curves to confirm the intrinsic activity of the catalysts (Fig. S4†). With the largest electrochemical active area, SnO$_2$@MoS$_2$ still has the best intrinsic activity compared to other samples. The measurement results of electrochemically active area show that

the construction of an interface layer in CC@SnO$_2$/MoS$_2$ nanosheets can effectively increase the number of active sites.

Furthermore, the hydrophilicity of electrode materials affects the performance of electrocatalytic hydrogen production. Hydrophilic samples can absorb more protons, and the H$_2$ generated on the surface is easier to desorb, which is more conducive to the occurrence of the HER. The surface wettability of CC@MoS$_2$ NS and CC@SnO$_2$/MoS$_2$ NS-2.5 samples was compared (Fig. S5A and B†). The surface of the CC@MoS$_2$ sample is hydrophobic and has weak adhesion to liquids. The CC@SnO$_2$/MoS$_2$ NS-2.5 sample turned into a surface hydrophilic material, which may be the result of the improvement of the overall material due to the hydrophilic nature of SnO$_2$. In addition, the electrical conductivity of the material has also been studied through the electrochemical impedance test, as shown in Fig. S6.† The electrochemical impedance test shows that the impedance of the SnO$_2$ nanosheet structure grown with MoS$_2$ nanoparticles is much smaller than that of pure MoS$_2$ and pure SnO$_2$ nanosheets, indicating that the construction of the SnO$_2$/MoS$_2$ interface layer speeds up electron transmission and reduces the resistance of the material. All these are further illustrated in the resistance fitting curve and equivalent circuit of the electrochemical impedance spectrum of SnO$_2$/MoS$_2$ (Fig. S7†).

As mentioned above, through the electron injection of SnO$_2$ into MoS$_2$, the design of the interface layer reduces the resistance of the lateral surface of MoS$_2$ to electron transfer and the strong van der Waals effect between layers to improve the conductivity. To study the electron transfer relationship between SnO$_2$ and MoS$_2$, the UV photoelectron spectroscopy (UPS) test of pure MoS$_2$ and pure SnO$_2$ was used to calculate their respective work functions (Φ). When an electron

transitions from the inside of the conductor to the outside of the conductor, the minimum energy value required is Φ. Therefore, electrons will be transferred from components with a small work function to components with a large work function, accelerating electron transport. The UV photoelectron spectroscopy shows the value of the Fermi edge (E_{Fermi}) and the truncated edge ($E_{cut\ off}$) of the sample, as shown in the formula.

$$\Phi = hv + E_{cut\ off} - E_{Fermi}$$

Among them, Φ is the work function of the material, also known as work function; hv is the monochromatic light source with a value of 21.2 eV. The UPS energy spectra of pure MoS$_2$ and pure SnO$_2$ are shown in Fig. 5A and B. The difference value of SnO$_2$ between the Fermi edge and the truncated edge is 11.43 eV (Fig. 5A). Similarly, for MoS$_2$, the calculation result of the difference value between the Fermi edge and the truncated edge is 10.21 eV (Fig. 5B). According to the formula, the work functions of SnO$_2$ NSs and MoS$_2$ NSs are 9.79 eV and 11.01 eV, respectively. The result shows that less energy is required for

electrons in SnO$_2$ to escape from the inside of the material to the surface of the material, which confirms the electron injection of SnO$_2$ into MoS$_2$ during the catalysis process. The previous performance test also demonstrates that this electron transfer does enhance the performance of the catalyst. The energy band structure and density of states (DOS) of SnO$_2$, MoS$_2$, and SnO$_2$/MoS$_2$ are also calculated to support the UPS test results, as shown in Fig. 5C and D. The theoretical calculation results of the energy band structure of SnO$_2$ and MoS$_2$ show that the band gap of SnO$_2$ is only 0.709 eV, showing excellent conductivity (Fig. 5C). In the conduction band position, the p orbit and s orbit of SnO$_2$ are more upward than those of MoS$_2$, which means that the electrons of SnO$_2$ are more easily transferred to the MoS$_2$ component, which is consistent with the results of UPS (Fig. 5D). Fig. 5E is the simulation diagram of SnO$_2$, MoS$_2$ and SnO$_2$/MoS$_2$ corresponding to the above theoretical calculation respectively. A simulation diagram of the electron transfer of the SnO$_2$/MoS$_2$ NS heterogeneous interface layer is shown in Fig. 6. Due to the small work function of SnO$_2$, electrons can be injected into the MoS$_2$ component at an accelerated rate, which increases the
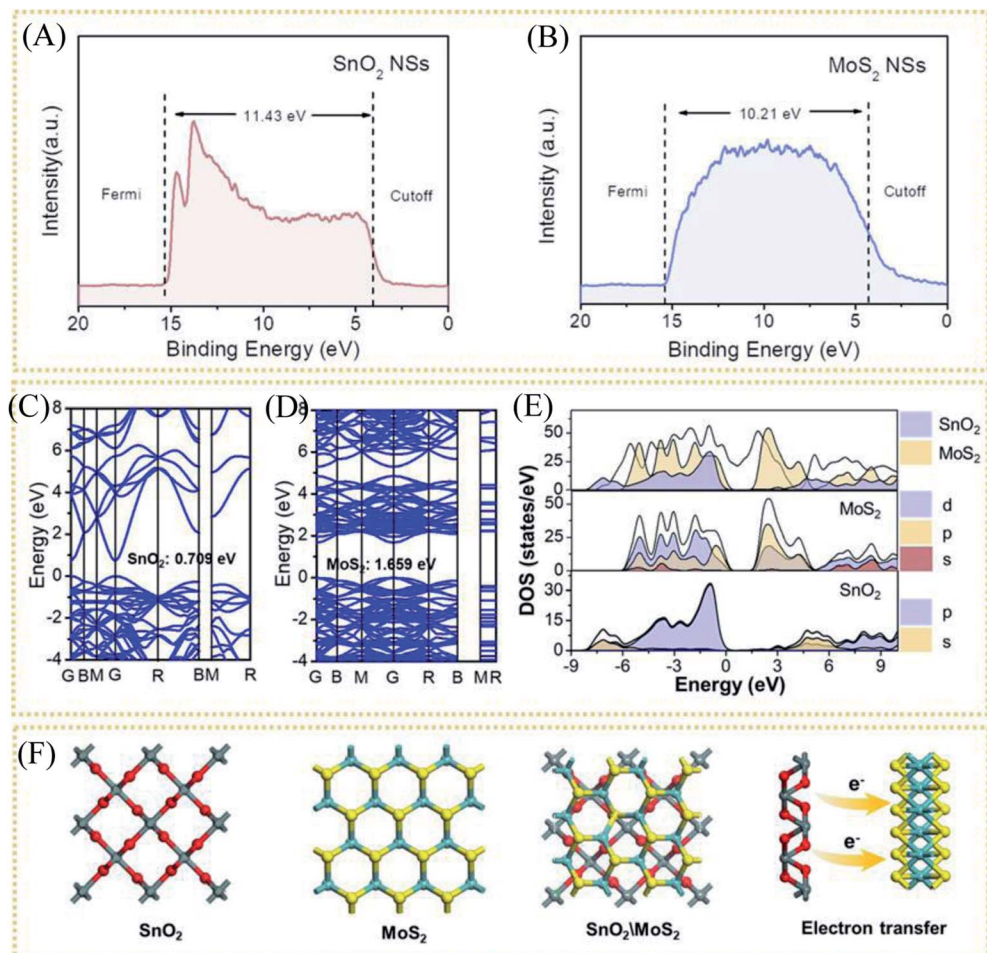

Fig. 5 Ultraviolet photoelectron spectroscopy (UPS) of (A) CC@SnO$_2$ NSs and (B) CC@SnS$_2$ NSs. (C) Calculation of band structure of SnO$_2$ and (D) MoS$_2$. (E) DOS and PDOS results for SnO$_2$, MoS$_2$ and SnO$_2$/MoS$_2$. (F) Modeling results of SnO$_2$, MoS$_2$ and SnO$_2$/MoS$_2$.
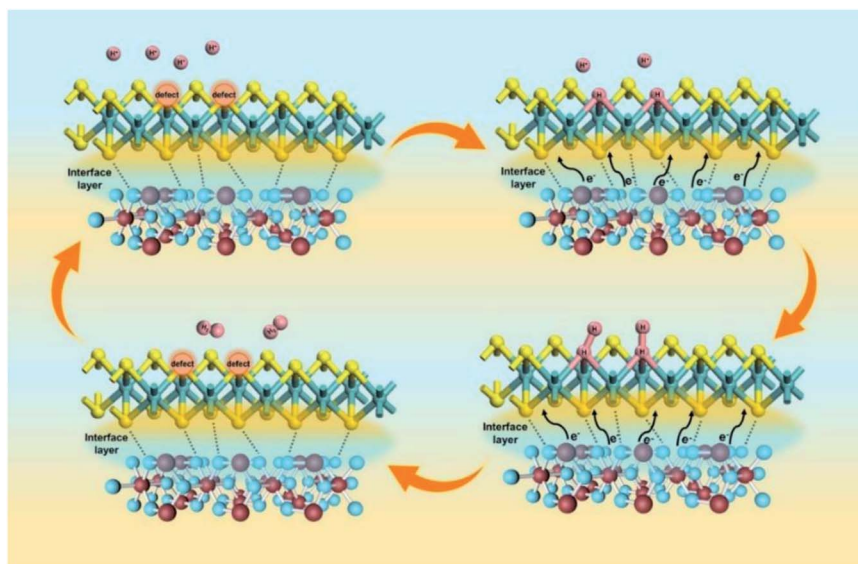
Fig. 6 Electron transfer simulation diagram of the SnO$_2$/MoS$_2$ NS heterogeneous interface layer.

electron transfer rate between the interface; on the other hand, due to the large amount of competing reactions in the reaction liquid unsaturated S atom defects, the structure of nanosheets/nanoparticles and the introduction of the SnO$_2$ increase the number of active sites and improve the hydrophilicity of the material, making H$^+$ easier to be adsorbed and reduced and H$_2$ desorbed.

Conclusions

To sum up, in order to construct an efficient and stable acidic HER electrocatalyst, using SnS$_2$ nanosheets on carbon cloth as the precursor, we transformed SnS$_2$ into SnO$_2$ with hydrophilia and corrosion resistance through the competitive reaction for S^{2-} between Mo^{4+} and Sn^{4+}. At the same time, MoS$_2$ nanoparticles were grown on SnO$_2$ nanosheets to obtain a SnO$_2$/MoS$_2$ interface layer with fast electron transfer and proton adsorption. The result of high-magnification TEM and XPS proved that the nanosheet/nanoparticle structure and the competitive reaction in the reaction solution increased the number of MoS$_2$ unsaturated sulfur defects and effectively prevented their aggregation; secondly, the interface contact angle test shows that the introduction of SnO$_2$ improved the overall hydrophilicity of the material, being beneficial to the HER; finally, the interface layer formed by SnO$_2$ and MoS$_2$ can accelerate the injection of electrons into molybdenum disulfide and reduce the resistance to electron transfer between molybdenum disulfide layers, which is proved by UPS and theoretical calculation. The typical SnO$_2$/MoS$_2$ heterogeneous nanosheets maintain good activity and stability in acid electrolytes. At a current density of 10 mA cm^{-2}, the overpotential of the SnO$_2$/MoS$_2$ is only 166 mV, having a significant performance improvement, compared with pure MoS$_2$, pure SnO$_2$ and pure SnS$_2$. We have proposed a strategy for constructing an interface layer with fast electron transport and proton adsorption, providing some new ideas for the design of HER catalysts in acid electrolytes.

Author contributions

Kun Huang: conceptualization, investigation, formal analysis, data curation, methodology, writing – original draft, and writing – review & editing. Lan Yang: conceptualization, investigation, formal analysis, data curation, and validation. Yihong Gao: theoretical calculation. Hui Zhang: methodology and investigation. Shikuo Li: methodology and investigation. Fangzhi Huang: conceptualization, data curation, formal analysis, funding acquisition, resources, and supervision.

Conflicts of interest

There are no conflicts to declare.

Acknowledgements

Notes and references

1 Y. Wang, H. Su, Y. He, L. Li, S. Zhu, H. Shen, P. Xie, X. Fu, G. Zhou, C. Feng, D. Zhao, F. Xiao, X. Zhu, Y. Zeng, M. Shao, S. Chen, G. Wu, J. Zeng and C. Wang, *Chem. Rev.*, 2020, **120**, 12217–12314.

2 T. Kosmala, A. Baby, M. Lunardon, D. Perilli, H. Liu, C. Durante, C. Di Valentin, S. Agnoli and G. Granozzi, *Nat. Catal.*, 2021, **4**, 850–859.

3 L. Schlapbach and A. Züttel, *Nature*, 2001, **414**, 353–358.

4 W. Yang and S. Chen, *Chem. Eng. J.*, 2020, **393**, 12472.

5 Q. Zhu, Y. Qu, D. Liu, K. W. Ng and H. Pan, *ACS Appl. Nano Mater.*, 2020, **3**, 6270–6296.

6 A.-L. Wang, H. Xu and G.-R. Li, *ACS Energy Lett.*, 2016, **1**, 445–453.

7 H. Cheng, Y.-Z. Su, P.-Y. Kuang, G.-F. Chen and Z.-Q. Liu, *J. Mater. Chem. A*, 2015, **3**, 19314–19321.

8 M. Gu, X. Deng, M. Lin, H. Wang, A. Gao, X. Huang and X. Zhang, *Adv. Energy Mater.*, 2021, **11**, 2102361.

9 X. Chen, J. Wan, J. Wang, Q. Zhang, L. Gu, L. Zheng, N. Wang and R. Yu, *Adv. Mater.*, 2021, **33**, 2104764.

10 N. Han, K. R. Yang, Z. Lu, Y. Li, W. Xu, T. Gao, Z. Cai, Y. Zhang, V. S. Batista, W. Liu and X. Sun, *Nat. Commun.*, 2018, **9**, 924.

11 X.-H. Lv, X.-Y. Wang, Y. Zhou, H. Xu and W.-M. Wan, *Chem. Commun.*, 2019, **55**, 9821–9824.

12 Z. Chen, H. Qing, R. Wang and R. Wu, *Energy Environ. Sci.*, 2021, **14**, 3160–3173.

13 A. P. Murthy, J. Madhavan and K. Murugan, *J. Power Sources*, 2018, **398**, 9–26.

14 Y. Dang, T. Wu, H. Tan, J. Wang, C. Cui, P. Kerns, W. Zhao, L. Posada, L. Wen and S. L. Suib, *Energy Environ. Sci.*, 2021, **14**, 5433–5443.

15 A. Li, H. Ooka, N. Bonnet, T. Hayashi, Y. Sun, Q. Jiang, C. Li, H. Han and R. Nakamura, *Angew. Chem., Int. Ed.*, 2019, **58**, 5054–5058.

16 J. Huang, H. Sheng, R. D. Ross, J. Han, X. Wang, B. Song and S. Jin, *Nat. Commun.*, 2021, **12**, 3036.

17 L. Wang, X. Duan, X. Liu, J. Gu, R. Si, Y. Qiu, Y. Qiu, D. Shi, F. Chen, X. Sun, J. Lin and J. Sun, *Adv. Energy Mater.*, 2020, **10**, 1903137.

18 J. Lim, D. Park, S. S. Jeon, C.-W. Roh, J. Choi, D. Yoon, M. Park, H. Jung and H. Lee, *Adv. Funct. Mater.*, 2018, **28**, 1704796.

19 P. Wang, X. Zhang, J. Zhang, S. Wan, S. Guo, G. Lu, J. Yao and X. Huang, *Nat. Commun.*, 2017, **8**, 14580.

20 J. Xu, C. Zhang, H. Liu, J. Sun, R. Xie, Y. Qiu, F. Lü, Y. Liu, L. Zhuo, X. Liu and J. Luo, *Nano Energy*, 2020, **70**, 104529.

21 X. Li, Y. Wang, J. Wang, Y. Da, J. Zhang, L. Li, C. Zhong, Y. Deng, X. Han and W. Hu, *Adv. Mater.*, 2020, **32**, 2003414.

22 W. Yang, S. Zhang, Q. Chen, C. Zhang, Y. Wei, H. Jiang, Y. Lin, M. Zhao, Q. He, X. Wang, Y. Du, L. Song, S. Yang, A. Nie, X. Zou and Y. Gong, *Adv. Mater.*, 2020, **32**, 2001167.

23 K. L. Zhou, C. Wang, Z. Wang, C. B. Han, Q. Zhang, X. Ke, J. Liu and H. Wang, *Energy Environ. Sci.*, 2020, **13**, 3082–3092.

24 V.-T. Nguyen, G.-J. Lee, Q.-T. Ngo, O. Omelianovych, N.-A. Nguyen, V.-H. Trinh, H.-S. Choi, A. Mnoyan, K. Lee, L. L. Larina and G. Chen, *Electrochim. Acta*, 2021, **398**, 139624.

25 T. Sun, J. Dong, Y. Huang, W. Ran, J. Chen and L. Xu, *J. Mater. Chem. A*, 2018, **6**, 12751–12758.

26 Y. Gao, Z. Chen, Y. Zhao, W. Yu, X. Jiang, M. He, Z. Li, T. Ma, Z. Wu and L. Wang, *Appl. Catal., B*, 2022, **303**, 120879.

27 S. Ali Shah, L. Xu, R. Sayyar, T. Bian, Z. Liu, A. Yuan, X. Shen, I. Khan, A. Ali Tahir and H. Ullah, *Chem. Eng. J.*, 2022, **428**, 132126.

28 H. Du, X. Zhang, Q. Tan, R. Kong and F. Qu, *Chem. Commun.*, 2017, **53**, 12012–12015.

29 G. Shao, X.-X. Xue, B. Wu, Y.-C. Lin, M. Ouzounian, T. S. Hu, Y. Xu, X. Liu, S. Li, K. Suenaga, Y. Feng and S. Liu, *Adv. Funct. Mater.*, 2020, **30**, 1906069.

30 L. Hu, X.-F. Song, S.-L. Zhang, H.-B. Zeng, X.-J. Zhang, R. Marks and D. Shan, *J. Catal.*, 2018, **366**, 8–15.

31 T. Ali, X. Wang, K. Tang, Q. Li, S. Sajjad, S. Khan, S. A. Farooqi and C. Yan, *Electrochim. Acta*, 2019, **300**, 45–52.

32 Q. He, S. Huang, M. Liu, P. Li, W. Sun and L. Hou, *Inorg. Chem. Front.*, 2020, **7**, 2660–2668.

33 B. Liu, Y. Cheng, B. Cao, M. Hu, P. Jing, R. Gao, Y. Du, J. Zhang and J. Liu, *Appl. Catal., B*, 2021, **298**, 120630.

34 Q. Zhang, H. Bai, Q. Zhang, Q. Ma, Y. Li, C. Wan and G. Xi, *Nano Res.*, 2016, **9**, 3038–3047.

35 X. Geng, W. Sun, W. Wu, B. Chen, A. Al-Hilo, M. Benamara, H. Zhu, F. Watanabe, J. Cui and T.-p. Chen, *Nat. Commun.*, 2016, **7**, 10672.

36 L. P. Hansen, Q. M. Ramasse, C. Kisielowski, M. Brorson, E. Johnson, H. Topsøe and S. Helveg, *Angew. Chem., Int. Ed.*, 2011, **50**, 10153–10156.

37 T. F. Jaramillo, K. P. Jørgensen, J. Bonde, J. H. Nielsen, S. Horch and I. Chorkendorff, *Science*, 2007, **317**, 100.

38 B. Hinnemann, P. G. Moses, J. Bonde, K. P. Jørgensen, J. H. Nielsen, S. Horch, I. Chorkendorff and J. K. Nørskov, *J. Am. Chem. Soc.*, 2005, **127**, 5308–5309.

39 X. Liu, B. Li, F. A. Soto, X. Li, R. R. Unocic, P. B. Balbuena, A. R. Harutyunyan, J. Hone and D. V. Esposito, *ACS Catal.*, 2021, **11**, 12159–12169.

40 T. Ren, W. Tian, Q. Shen, Z. Yuan, D. Chen, N. Li and J. Lu, *Nano Energy*, 2021, **90**, 106527.

41 L. Guo, Q. Liu, Y. Liu, Z. Chen, Y. Jiang, H. Jin, T. Zhou, J. Yang and Y. Liu, *Nano Energy*, 2022, **92**, 106707.

42 S. Ravula, C. Zhang, J. B. Essner, J. D. Robertson, J. Lin and G. A. Baker, *ACS Appl. Mater. Interfaces*, 2017, **9**, 8065–8074.

43 S. Ji, Z. Yang, C. Zhang, Z. Liu, W. W. Tjiu, I. Y. Phang, Z. Zhang, J. Pan and T. Liu, *Electrochim. Acta*, 2013, **109**, 269–275.

44 E. W. Keong Koh, C. H. Chiu, Y. K. Lim, Y.-W. Zhang and H. Pan, *Int. J. Hydrogen Energy*, 2012, **37**, 14323–14328.

45 X. Zhou, Y. Liu, H. Ju, B. Pan, J. Zhu, T. Ding, C. Wang and Q. Yang, *Chem. Mater.*, 2016, **28**, 1838–1846.

46 J. Wu, R. Zhao, H. Xiang, C. Yang, W. Zhong, C. Zhang, Q. Zhang, X. Li and N. Yang, *Appl. Catal., B*, 2021, **292**, 120200.

47 S. Ravula, C. Zhang, J. B. Essner, J. D. Robertson, J. Lin and G. A. Baker, *ACS Appl. Mater. Interfaces*, 2017, **9**, 8065–8074.

48 G. Liu, Y. Qiu, Z. Wang, J. Zhang, X. Chen, M. Dai, D. Jia, Y. Zhou, Z. Li and P. Hu, *ACS Appl. Mater. Interfaces*, 2017, **9**, 37750–37759.

49 X. Xiao, Y. Wang, X. Xu, T. Yang and D. Zhang, *Mol. Catal.*, 2020, **487**, 110890.

50 Y. Huang, Y.-E. Miao, L. Zhang, W. W. Tjiu, J. Pan and T. Liu, *Nanoscale*, 2014, **6**, 10673–10679.

51 Y. Yu, J. Xu, J. Zhang, F. Li, J. Fu, C. Li and C. An, *Nanomaterials*, 2020, **10**, 2337.

52 I. Roger, R. Moca, H. N. Miras, K. G. Crawford, D. A. J. Moran, A. Y. Ganin and M. D. Symes, *J. Mater. Chem. A*, 2017, **5**, 1472–1480.